Nano Research

Open Access

Communication

Asymmetric B-coordination stimulated high-spin cobalt boosts ORR

Yugang Qi[1], Kexin Song[1], Qing Liang[1], Xinyan Zhou[1], Meiqi Liu[1], Wenwen Li[1], Fuxi Liu[1], Zhou Jiang[1], Qinhua Gu[2], Zhongjun Chen[3], Bingsen Zhang[2] ✉, and Wei Zhang[1] ✉

[1] *Key Laboratory of Automobile Materials MOE, School of Materials Science & Engineering, Electron Microscopy Center, and International Center of Future Science, Jilin Provincial International Cooperation Key Laboratory of High-Efficiency Clean Energy Materials, Jilin University, Changchun 130012, China*
[2] *Shenyang National Laboratory for Materials Science, Institute of Metal Research, Chinese Academy of Sciences, Shenyang 110016, China*
[3] *Institute of High Energy Physics, Chinese Academy of Sciences, Beijing 100049, China*

Cite this article: *Nano Research*, **2025**, *18*, 94907278. https://doi.org/10.26599/NR.2025.94907278

ABSTRACT: As affordable electrocatalysts for oxygen reduction reactions (ORR) in metal-air batteries, nitrogen-carbon supported atomically dispersed single-atom transition-metal electrocatalysts are emerging. Accurately modulating the first-shell coordination of single-atom metal sites remains challenging, which impedes the elucidation of geometric/electronic structures for optimizing ORR catalysts. Aiming to tackle this challenge by rational design and constructing an asymmetric coordination model catalyst Co-B/N-C, herein we unravel that asymmetric B-coordination stimulates the generation of Co high spin state ($t_{2g}5e_g2$). By using X-ray absorption spectroscopy (XAS), we confirm Co active sites are atomically dispersed with a first-shell coordination of boron and nitrogen atom (Co-B_1N_3). Thus, the adsorption strength and electron transfer between the cobalt centers and the reactants/intermediates were boosted for optimal ORR capacity ($E_{1/2}$ = 0.87 V). Our work will provide valuable new perspectives on the strategic development of high-performance magnetic metal catalysts for ORR.

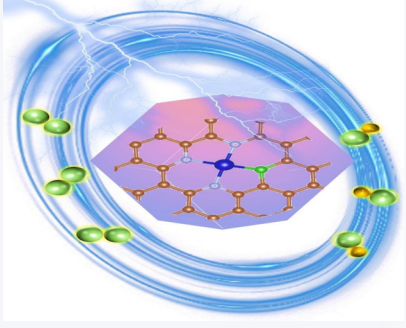

KEYWORDS: electrocatalysis, oxygen reduction reaction, single atom catalyst, spin state

1 Introduction

As emerging catalysts, single-atom catalysts (SACs) demonstrated enormous potential in thermo-electrocatalysis due to distinctive chemical surroundings and optimal utilization of central metal [1–7]. Monometallic-modified amorphous carbon has been experimentally and theoretically proven to be an outstanding oxygen electrocatalyst [8–10]. Due to its outstanding catalytic activity for oxygen reduction reactions (ORR), Fe-N-C stands out among the numerous metal-nitrogen-carbon (M-N-C) catalysts, yet it suffers from significant activity degradation attributed to the Fenton effect [11–16]. Interestingly, Co-N-C emerges as promising SACs for ORR, as predicted by the high theoretical activity of the volcano diagram [17]. Hence, it is crucial to experimentally and theoretically pinpoint the active sites of Co-N-C SACs towards architecting superior ORR performance.

When designing high-performance SAC, it is essential to concurrently take both the central metals and local coordination environment into consideration [18–23]. Reactant adsorption and conversion into products on the catalyst surface are reaction processes in heterogeneous catalysis [24–27]. Therefore, the binding energy magnitude of the intermediate and a catalyst is crucial to control the catalytic process. The former is governed by the electronic configuration of the active site, and the alteration of the local coordination environment enables an effective regulation of the electronic structure [28–33]. The standard symmetric planar four-coordination structure has been experimentally proven to constitute the optimal active site for catalytic processes [34, 35]. For the MN_4 part, the high electronegativity of nitrogen atoms symmetrically adjacent to metal center results in adverse free energy changes for intermediate adsorption [36–38]. Thus, it is essential but challenging to accurately manipulate the geometry and electronic properties of Co-N-C catalysts to optimize the binding energy of those key intermediates. However, due to the good thermodynamic stability of the Co-N_4 structure, it is a great challenge for the introduction of heteroatoms in Co-N-C to replace the first shell layer N ligand. *In situ* boronization was performed, providing an opportunity to uniformly tailor the coordination environment around metal atoms with B atoms. As a consequence, such an approach can be used to alter the adsorption intensity of ORR intermediates at the active site by adjusting the interfacial

Received: December 26, 2024; **Revised:** January 24, 2025
Accepted: January 27, 2025

✉Address correspondence to Wei Zhang, weizhang@jlu.edu.cn; Bingsen Zhang, bszhang@imr.ac.cn

configuration of one central metal atom, yielding the boosted catalytic activity [39].

Herein, a nuanced strategy was developed to meticulously tailor the coordination milieu and electronic state of Co sites. A novel catalyst, noted as Co-B/N-C, exhibits high potential for the ORR. Boron incorporation induces electron delocalization in Co, facilitating a spin state from low-spin ($t_{2g}6e_g1$) to high-spin ($t_{2g}5e_g2$) configuration, which enhances π-orbital overlap with oxygen antibonding orbitals. This results in enhanced ORR performance in alkaline media. Moreover, density functional theory (DFT) calculations reveal that asymmetric B can enhance the adsorption of ORR intermediates on the Co site, which promotes the kinetic process of ORR by reducing the theoretical overpotentials. Ultimately, Co-B/N-C catalyst has demonstrated outstanding performance in zinc-air battery (ZAB) applications.

2 Results and discussion

2.1 Preparation of Co-B/N-C

Co-B/N-C was produced via chemical co-precipitation followed by pyrolysis (Fig. 1(a)). It is noteworthy that Zn was evaporated (> 907 °C) [40, 41], suggesting a minimal influence of Zn species on catalytic activity [42]. As comparisons, Co-N-C, N-B-C, and N-C were derived from a comparable approach. Details are given in the Electronic Supplementary Material (ESM).

2.2 Morphological and structural analysis of Co-B/N-C

To verify that the introduction of source B exists as discrete molecular species, X-ray diffraction (XRD) test was conducted on the samples. The XRD curve reveals that the introduction of B did not disrupt the original crystal structure (Fig. S1 in the ESM). Thermogravimetric analysis also showed that the catalyst exhibited excellent thermal stability after the introduction of B (Fig. S2 in the ESM). By transmission electron microscopy (TEM), Fig. 1(b) showed that Co-B/N-C roughly maintained the polyhedral shape with a diameter of ~ 500 nm. High-resolution TEM (HRTEM) image and selected area electron diffraction (SAED) demonstrate the absence of Co particles (Fig. 1(c)). Hence, the Co species are likely dispersed as isolated atoms on the amorphous NC substrate. Distinct graphitic carbon layers in the porous skeleton can be observed, which contributes to the improvement of the electrical

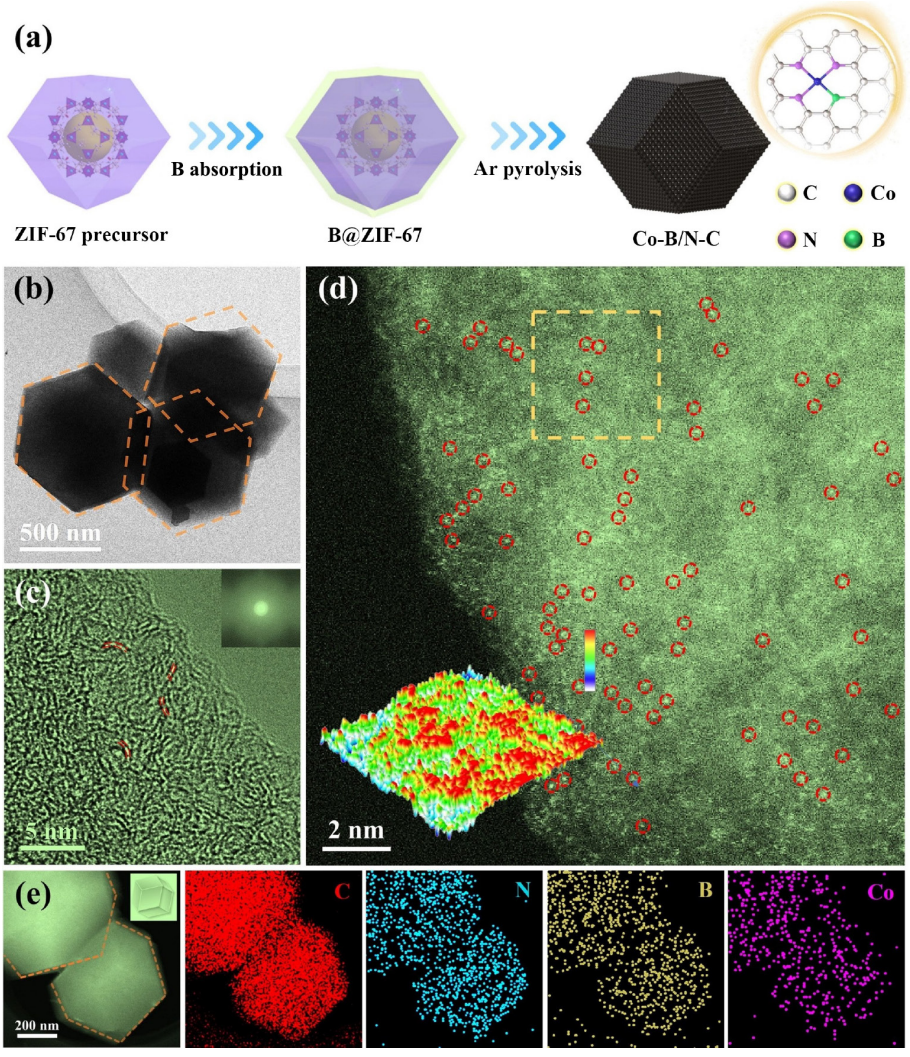

Figure 1 Preparation and electron microscopy of Co-B/N-C. (a) Schematics of preparation procedure. (b) TEM image, (c) HRTEM image and corresponding SAED (inset), and (d) HAADF-STEM image for Co-B/N-C, indicating single-atom loading on the carbon support. The inset shows a 3D intensity surface plot and intensity range displayed for the yellow region in (d). (e) EDS elemental mapping images of Co-B/N-C.

conductivity [43, 44]. The low crystallinity post-pyrolysis suggests a high density of defects within the carbon matrix (Fig. S3 in the ESM), which promotes the immobilization of isolated metal ions. Raman analysis (Fig. S4 in the ESM) was involved by applying the correlative Raman/scanning electron microscopy (SEM) technique [45]. Further results support the existence of widespread defective disordered carbon [46]. Defective-to-graphitic carbon band intensity ratio (D/G) for Co-B/N-C is similar to all the control samples, indicating that the carbon substrate has not been destroyed. High-angle annular dark-field scanning TEM (HAADF-STEM) images display the uniform scattering of bright spots on the substrate (Fig. 1(d)), which indicate atomic-level dispersion of Co atoms marked with red circles [47]. Meanwhile, the inset shows the three-dimensional (3D) intensity of Co atoms. Nevertheless, the B atom is not distinctly resolved because of its low atomic number. Energy-dispersive X-ray spectroscopy (EDS) (Fig. 1(e)) indicated the uniform presence of C, N, Co, and B throughout the architecture. Due to superior mechanical strength and thermal stability, the catalyst maintained its structure after heat treatment, with control samples exhibiting similar outcomes (Figs. S5–S7 in the ESM). Based on the inductively coupled plasma mass spectrometry (ICP-MS) results, the Co-B/N-C contained 1.37 wt.% Co and 0.15 wt.% B, respectively. The control sample presents a similar weight percentage (Table S1 in the ESM). The surface area and pore size characteristics of Co-B/N-C and Co-N-C were obtained by isothermal nitrogen adsorption–desorption measurements (Figs. S8 an S9 in the ESM). Brunauer–Emmett–Teller (BET) results show that the introduction of B contributes to the formation of defects, thus increasing the specific surface area [48]. The large surface area of Co-B/N-C is predicted to increase active sites exposure, and the mesopores are able to improve mass transfer during catalysis, which leads to the enhancement of catalytic activity [49].

2.3 Electronic interactions and atomic coordination structure of Co-B/N-C

Coordination structure details were examined through X-ray photoelectron spectroscopy (XPS) and X-ray absorption fine spectroscopy (XAFS). XPS survey spectrum of Co-B/N-C displayed in Fig. S10 in the ESM demonstrated the existence of C, N, O, Co, and B elements. The C 1s spectrum (Fig. S11 in the ESM) is distinctly categorized into three principal peaks of 288.4, 284.7, and 285.7 eV, corresponding to the C–C, C=C, and C=N bonds, respectively [50–52]. This confirmed the graphene-like nature of the carbon support for Co-B/N-C. Meanwhile, soft X-ray emission spectrometer (SXES) spectra of C K_{α}-edge were obtained to reveal the electronic structure of carbon (Fig. S12 in the ESM). After the introduction of B, the C K_{α}-edge peak shifts towards higher energy (139.26–139.42 eV), indicating local electron acceleration of graphitic layers [53, 54]. High-resolution N 1s spectrum (Fig. S13 in the ESM) shows four main peaks of 398.3, 399.2, 400.9, and 403.7 eV, corresponding to pyridinic N, Co–N, pyrrolic N, and graphitic N [55–57]. Besides, a summary of the proportions and quantities of the four nitrogen species is provided (Table S2 in the ESM). The higher content of pyridinic N and pyrrolic N in Co-B/N-C preferred the ORR reaction [58–60]. The B 1s spectrum (Fig. S14 in the ESM) of Co-B/N-C exhibits two major peaks: B–C species (191.65 eV) [61] and B–Co species (188.15 eV) [62, 63]. The presence of the B–Co bond indicates that the B atom prefers direct coordination with Co atom. The Co 2p orbital (Fig. S15 in the ESM) can be assigned to two main peaks of Co $2p_{3/2}$ (780.8 eV) and Co $2p_{1/2}$ (796.5 eV). The positive shift of Co $2p_{3/2}$ in Co-B/N-C signifies a high valence with Co.

XAFS analyses were conducted to elucidate the atomic-scale chemical speciation and coordination sphere of Co. The K-edge X-ray absorption near-edge structure (XANES) spectra of Co (Fig. 2(a)) demonstrate that the near-edge absorption edge of Co in Co-N-C and Co-B/N-C specimen situated between the Co foil and Co_3O_4, illustrating the valence of Co is between 0 and +3 [64, 65]. The Co oxidation state was ascertained through the analysis and fitting of K-edge XANES spectra (Fig. S16 in the ESM). Critically, Co has higher binding energy in Co-B/N-C compared to Co-N-C, which parallels the XPS and EXAFS conclusions. To investigate the coordination configurations of the Co site, the k_3-weighted Fourier transform of Co K-edge extended X-ray absorption fine structure (FT-EXAFS) spectra in *R*-space were employed (Fig. 2(b)). Our analysis revealed a distinct FT peak at 1.44 Å in the sample, primarily due to scattering from Co–N and Co–B coordination. By contrast with other FT-EXAFS spectra, this signal in Co-B/N-C was considered owing to Co–B scattering, indicating the formation of Co–B bonding. The structural parameters from the Co K-edge were quantitatively determined using least-square EXAFS fitting (Fig. 2(c)). The results show that the first-layer coordination number of the central atom Co is 4, which is bonded to one B atom and three N atoms, with average bond lengths of 1.91 and 1.83 Å, respectively (Table S3 in the ESM). The control samples also show good fitting results (Figs. S17–S21 in the ESM). The Co K edge wavelet transform (WT)-EXAFS was employed to characterize the atomic configuration of Co-B/N-C, owing to its superior resolution in *k* and *R* spaces (Figs. 2(d)–2(f)). As displayed in Fig. 2(f), the WT result of Co-B/N-C exhibits a single intensity maximum at ~ 5.5 $Å^{-1}$, which is close to the Co–N–C. The absence of Co–Co coordination further confirmed the discrete nature of Co species in Co–B/N–C (Figs. S22 and S23 in the ESM).

The electron spin configuration in Co-B/N-C was probed via temperature-dependent magnetic susceptibility measurements [66, 67]. The effective magnetic moments were calculated to be 4.12 and 2.15 μ_{eff} for Co-B/N-C and Co-N-C, respectively (Figs. 2(g) and 2(h)). Moreover, the number of unpaired *d* electrons (*n*) of the Co ion was further obtained by the equation. Whereby the Co-N–C has 1.3 unpaired *d* electrons, indicating that the Co ion is under low spin (LS) with one e_g filling. Unpaired *d* electron (*n*) of Co-B/N-C is 3.3, which has two e_g filling under a high spin (HS) state. These findings suggest that modifying the Co coordination environment alters its electronic structure and spin state. The schematic diagram of the atomic interface model for Co-B/N-C also corresponds to the fitting results (Fig. 2(i)).

2.4 ORR activity of Co-B/N-C

The ORR activity of Co-B/N-C was assessed in a standard three-electrode system. Figure 3(a) displays the linear sweep voltammetry (LSV) curves of various electrocatalysts. Co-B/N-C shows optimum ORR performance (E_{onset} = 0.95 V, $E_{1/2}$ = 0.87 V, and *j* = 5.25 mA·cm^{-2}), exceeding 20% Pt/C and the majority of documented electrocatalysts (Table S4 in the ESM). It is known that half-wave potential is tightly linked to the catalyst's inherent activity. When contrasted with Co-N-C, Co-B/N-C exhibits superior half-wave potential, proving that B doping substantially improved catalyst intrinsic activity. The presence of both Co and B

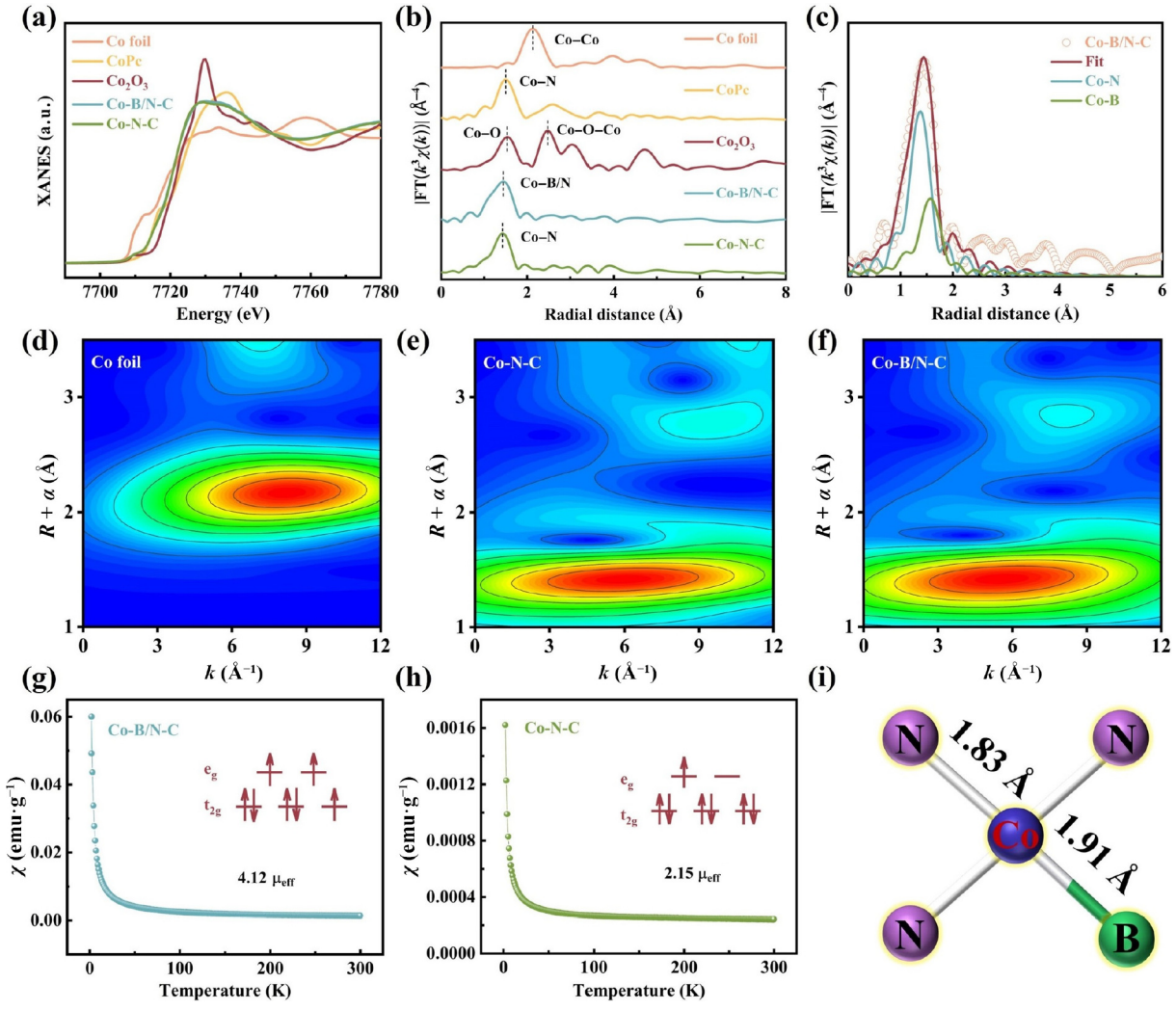

Figure 2 Atomic configuration and spin states of Co-B/N-C. (a) Co K-edge XANES spectra. (b) FT EXAFS spectra. (c) FT-EXAFS fitting curves of Co-B/N-C. (d)–(f) WT-EXAFS plots of different samples. Magnetic susceptibility of (g) Co-B/N-C and (h) Co-N-C. (i) Schematics of atomic interface model for Co-B/N-C.

improves electron transfer, leading to enhanced ORR performance. The kinetics of the synthesized electrocatalysts were probed through comparative Tafel analysis, as depicted in Fig. 3(b). Co-B/N-C exhibits the lowest Tafel slope (75.4 mV·dec^{-1}), elucidating the fastest ORR reaction kinetics [68]. Smaller values of electrochemical impedance favor the mass transfer process (Fig. S24 in the ESM). Furthermore, Co-B/N-C outperforms other catalysts across multiple electrochemical metrics (Fig. 3(c)). To explore the corresponding ORR mechanism, LSV curves obtained at various rotation speeds were examined (Fig. S25 in the ESM). The ORR selectivity of Co-B/N-C was clarified using rotating ring-disk electrode (RRDE) polarization curves (Fig. 3(d)). The corresponding H_2O_2 yield (H_2O_2%) and electron transfer number (n) of Co-B/N-C confirm that ORR predominantly follows a four-electron transfer mechanism (n = 3.9) (Fig. 3(e)).

Both stability and methanol tolerance are the pivotal descriptors that determine the practical application of electrocatalysts. The current density remains largely unaffected after methanol introduction, indicating good methanol tolerance (Fig. S26 in the ESM). Simultaneously, durability was assessed through an accelerated degradation test (ADT). The as-developed Co-B/N-C shows exceptional stability with minimal $E_{1/2}$ loss after 3000 continuous CV cycles (Fig. 3(f)). Larger electrochemical active surface area (ECSA) offers more active sites thereby enhancing the catalytic activity (Fig. 3(g) and Fig. S27 in the ESM). Co-B/N-C showed extraordinary performance when compared to most of the reported catalysts (Fig. 3(h)). The extremely high stability of Co-B/N-C may be attributed to the high spin of Co ($t_{2g}5e_g2$) and the stable architecture.

2.5 Electrochemical performance of the fabricated Zn–air batteries

To showcase the practical energy device potential of Co-B/N-C electrocatalyst, we evaluated a ZAB using it as the cathode. Meanwhile, another ZAB containing Pt/C was used as a control (Fig. 4(a)). The Co-B/N-C ZAB achieved an open circuit voltage (OCV) of 1.43 V (Fig. 4(b)), and its ability to illuminate light-emitting devices (LEDs) (inset) underscores its potential for practical electronic applications. Furthermore, the Co-B/N-C based ZAB delivered a specific capacity of 802.3 mAh·g_{Zn}^{-1}, adjacent to theoretical value (820 mAh·g_{Zn}^{-1}, Fig. 4(c)). The peak power density achieved 148.6 mW·cm^{-2}, surpassing the 20% Pt/C based ZAB (Fig. 4(d)). The full discharge curves at various current densities also validate its sustainability as practical electronic device (Fig. S28

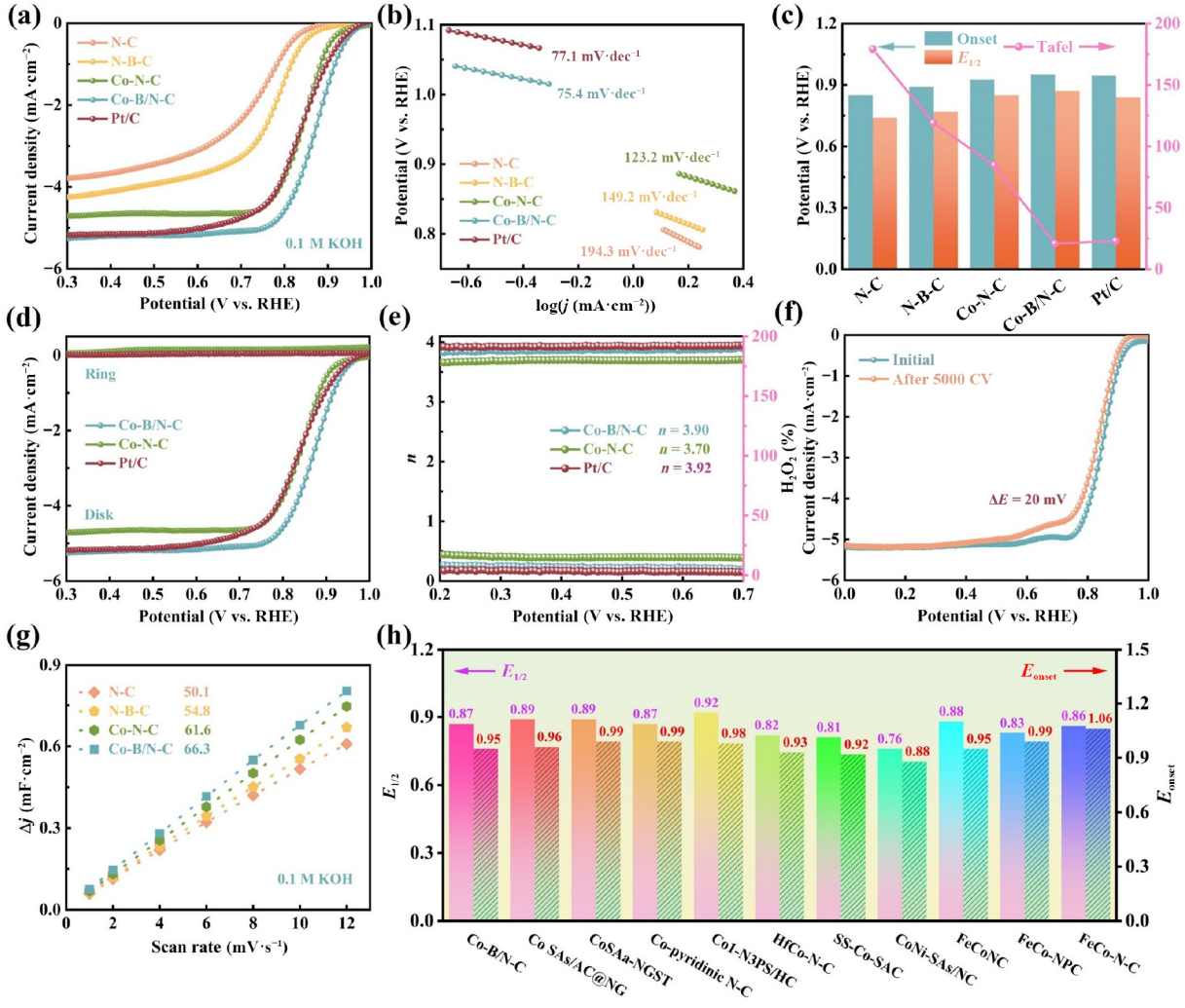

Figure 3 Polarization curves for ORR of Co-B/N-C and reference samples. (a) Polarization curves for Co-B/N-C and the references. (b) Tafel plots. (c) Comparison of Tafel, E_{onset}, and $E_{1/2}$ of different samples. (d) ORR curves of the electrocatalysts tested by RRDE. (e) H_2O_2 yield and electron transfer number (n). (f) LSV curves of Co-B/N-C before and after CV testing. (g) ECSA curve corresponding with catalysts. (h) Comparison of activity between target catalyst and most reported catalysts.

in the ESM). The rate performance of two ZABs was further evaluated (Figs. 4(e) and 4(f)). The Co-B/N-C-based ZAB demonstrated a stable and higher discharge voltage plateau than the 20% Pt/C-based ZAB at various current densities, demonstrating enhanced rate capability and durability. The slight change in potential difference after 400 cycles demonstrates extraordinary cycling performance (Fig. 4(g) and Fig. S29 in the ESM). This result demonstrates the excellent rechargeability and multiplier performance with Co-B/N-C, primarily attributed to the favorable catalytic performance and robust stability.

2.6 Theoretical study of Co-B/N-C on ORR

To delve into the atomic-level mechanisms behind the superior ORR behavior of Co-B/N-C, we conducted DFT calculations to analyze their electronic configuration, bonding characteristics, and adsorption energy. DFT calculation model derived from the previous analysis and the EXAFS fitting results (Fig. S30 in the ESM). Figure 5(a) illustrates the atomic schemes and electronic structures of Co-N-C and Co-B/N-C. The controlled modulation of Co spin states from weak to strong styles is achieved by manipulating the atomic substitution, regulating the Co spin state from LS to HS. The disparity in charge density at the Co center in the presence and absence of B was examined to elucidate the function of B. As shown in Fig. 5(b), after introducing B, the charge density of the Co center rises, which is due to the lower electronegativity of B (2.04) compared to N (3.04). For M-N-C catalysts with weaker adsorption performance, the enhanced charge density of the catalytic site facilitates the adsorption with ORR intermediates. The central Co charge state is quantified using Bader charge analysis (Fig. 5(c)). The ΔG_{O^*} decreases as the Bader charge increases, suggesting a stronger interaction with adsorbed oxygen in Co-B/N-C compared to Co-N-C, which may indicate improved ORR catalytic activity. Gibbs free energy profiles for Co-B/N-C and Co-N-C at U = 0 and 1.23 V are shown in Figs. 5(d) and 5(e), respectively. Relative to Co-N-C, Co-B/N-C exhibits lower adsorption energy for intermediates in the ORR process. This suggests that B incorporation enhances the adsorption of ORR intermediates on the Co site, resulting in a reduction of theoretical overpotential. In addition, the presence of B reduces the overpotential of the reaction by 0.56 V. Figure 5(f) shows the projected density of states (PDOS) for d orbitals of Co-B/N-C. Owing to the incorporation of the coordinated B, the Co atom in the Co-B/N-C had more electrons that occupied the $d_{x^2-y^2}$ orbital than that of Co-N-C (Fig. S31 in the ESM). Dramatically, the

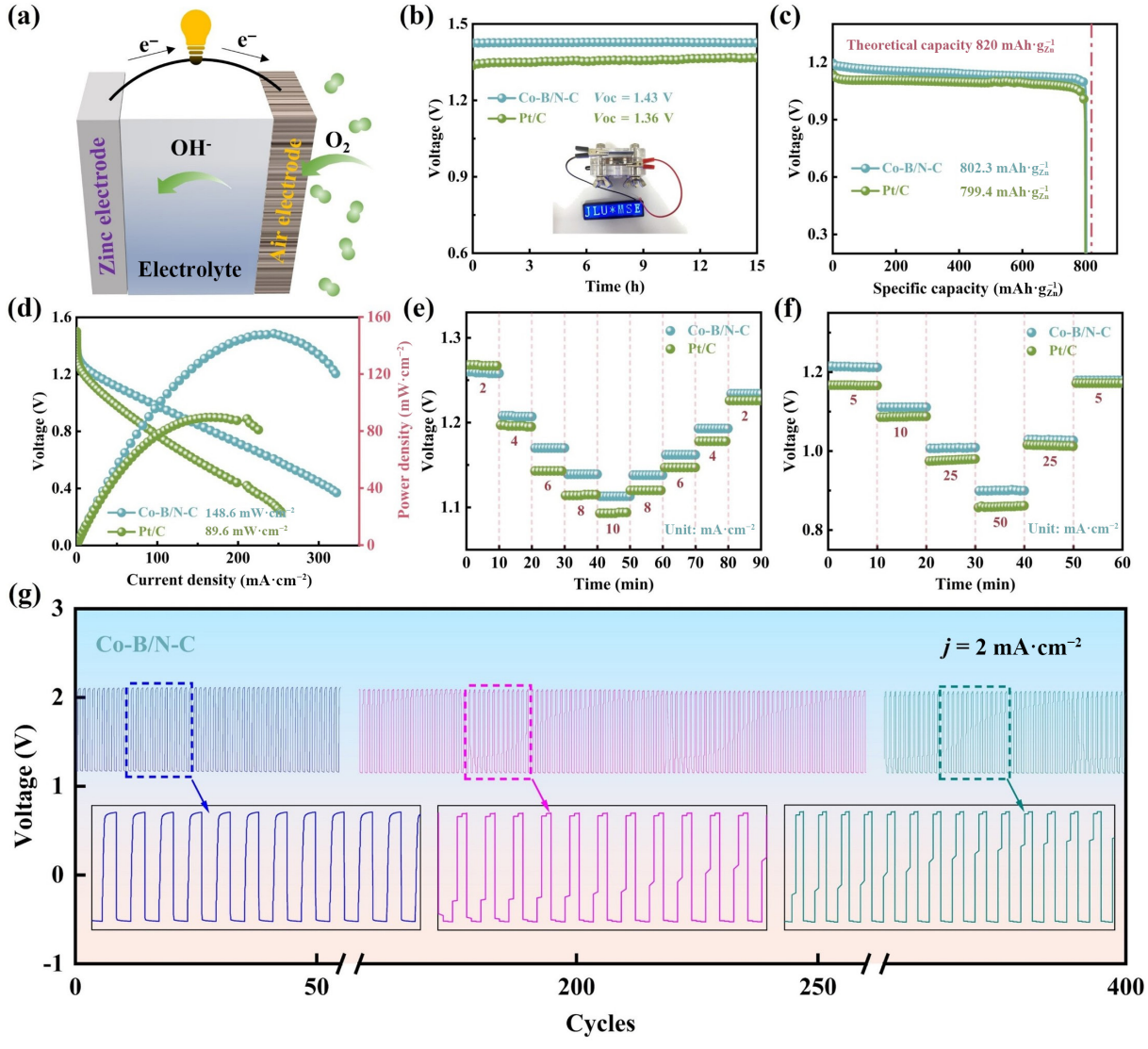

Figure 4 Performance assessment of Co-B/N-C based ZAB. (a) Graphical representation of ZAB. (b) Corresponding OCV curve. (c) Constant current discharge curve and specific capacity. (d) Polarization and power density plots for discharge. Constant current charge–discharge curves (e) and (f). (g) Stability test (10 min for one cycle).

additional π bonds contributed from the Co $d_{x^2-y^2}$ orbitals strengthened the weak bonding of ORR intermediates (Fig. 5(g) and Fig. S32 in the ESM), leading to an enhancement in ORR performance of Co centers.

3 Conclusions

In summary, we synthesized a single-atom Co-based ORR electrocatalyst featuring unsymmetrical Co-B/N-C complexes within MOF-derived hierarchically porous carbon frameworks via atomic interface engineering. Our thorough research reveals that the spin-state configuration of 3d orbitals in transition metals is crucial for enhancing ORR performance. Electron configuration characteristics and theoretical calculations both indicate that the adjacent dispersed B atoms can effectively activate the Co sites and permits an ideal electron ($t_{2g}5e_g2$) filling, which facilitates easy penetration of the antibonding π-orbital of oxygen, contributing to the superior ORR performance of Co-B/N-C. The optimized electronic structure and constrained charge behaviors aid in modulating the adsorption of oxygenate intermediates, thus enhancing oxygen electrocatalysis. Our work offers significant insights into orbital interaction and charge behaviors, which provide valuable guidance for designing high-performance catalysts.

Electronic Supplementary Material: Supplementary material (materials and methods, experimental section, characterization, electrochemical measurements, computational details, and EXAFS fitting) is available in the online version of this article at https://doi.org/10.26599/NR.2025.94907278.

Data availability

All data needed to support the conclusions in the paper are presented in the manuscript and the Electronic Supplementary Material. Additional data related to this paper may be requested from the corresponding author upon request.

Acknowledgements

This work was supported by the National Natural Science Foundation of China (Nos. 12234018 and 51872115) and Beijing Synchrotron Radiation Facility (BSRF) 4B9A.

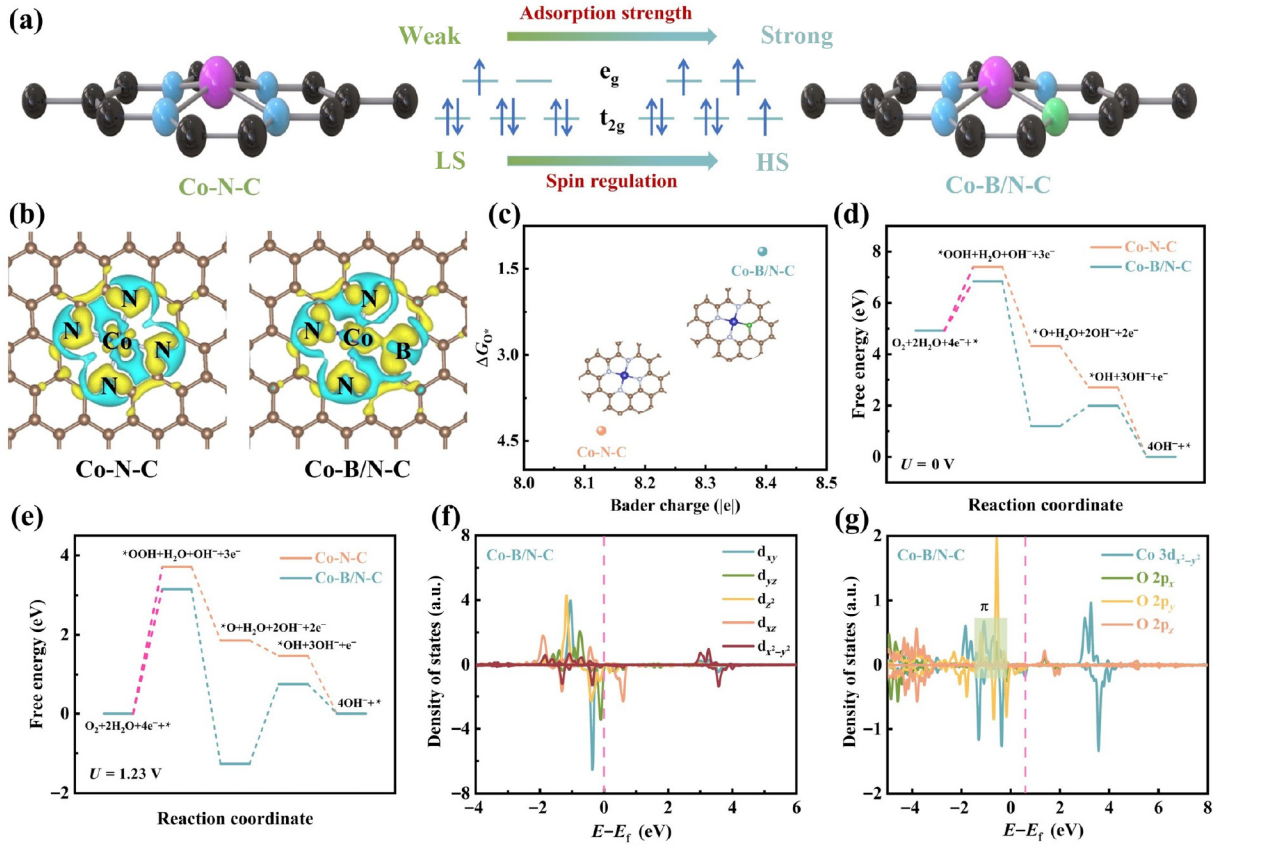

Figure 5 Theoretical ORR activity of Co-B/N-C. (a) Atomic schemes and electronic structures of Co-N-C and Co-B/N-C. (b) Differences in charge density between Co-N-C and Co-B/N-C. (c) Bader charge of Co and ΔG_{O^*} for Co-N-C and Co-B/N-C. Gibbs free energy profile for ORR process of the (d) and (e) at the U = 0 V and U = 1.23 V. Projected density of states of Co sites and O sites of Co-B/N-C (f) and (g).

Declaration of competing interest

All the contributing authors state that they have no conflict of interests in this work.

Author contribution statement

Y. G. Q.; Writing – original draft, experimental design, validation, data curation, conceptualization. K. X. S.: Data curation. Q. L.: Data curation. X. Y. Z.: Data curation. M. Q. L.: Data curation. W. W. L.: Data curation. F. X. L.: Data curation. Z. J.: Data curation. Q. H. G.: Data curation. Z. J. C.: Data curation. B. S. Z.: Writing – review & editing, supervision. W. Z.: Writing – review & editing, conceptualization, funding acquisition, supervision.

Use of AI statement

None.

References

[1] Zhang, W.; Zheng, W. T. Single atom excels as the smallest functional material. *Adv. Funct. Mater.* **2016**, *26*, 2988–2993.

[2] Fei, H. L.; Dong, J. C.; Chen, D. L.; Hu, T. D.; Duan, X. D.; Shakir, I.; Huang, Y.; Duan, X. F. Single atom electrocatalysts supported on graphene or graphene-like carbons. *Chem. Soc. Rev.* **2019**, *48*, 5207–5241.

[3] Zhang, N. Q.; Ye, C. L.; Yan, H.; Li, L. C.; He, H.; Wang, D. S.; Li, Y. D. Single-atom site catalysts for environmental catalysis. *Nano Res.* **2020**, *13*, 3165–3182.

[4] Gawande, M. B.; Fornasiero, P.; Zbořil, R. Carbon-based single-atom catalysts for advanced applications. *ACS Catal.* **2020**, *10*, 2231–2259.

[5] Kim, H.; Shin, D.; Yang, W.; Won, D. H.; Oh, H. S.; Chung, M. W.; Jeong, D.; Kim, S. H.; Chae, K. H.; Ryu, J. Y. et al. Identification of single-atom Ni site active toward electrochemical CO_2 conversion to CO. *J. Am. Chem. Soc.* **2021**, *143*, 925–933.

[6] Xue, W. X.; Zhu, Z. W.; Chen, S. X.; You, B.; Tang, C. H. Atomically dispersed Co-N/C catalyst for divergent synthesis of nitrogen-containing compounds from alkenes. *J. Am. Chem. Soc.* **2023**, *145*, 4142–4149.

[7] Wu, Q. Y.; Zhou, R. X.; Yao, Z. Y.; Wang, T. Y.; Li, Q. Effective approaches for enhancing the stability of ruthenium-based electrocatalysts towards acidic oxygen evolution reaction. *Chin. Chem. Lett.* **2024**, *35*, 109416.

[8] Wagner, S.; Auerbach, H.; Tait, C. E.; Martinaiou, I.; Kumar, S. C. N.; Kübel, C.; Sergeev, I.; Wille, H. C.; Behrends, J.; Wolny, J. A. et al. Elucidating the structural composition of an Fe-N-C catalyst by nuclear- and electron-resonance techniques. *Angew. Chem., Int. Ed.* **2019**, *58*, 10486–10492.

[9] Zitolo, A.; Ranjbar-Sahraie, N.; Mineva, T.; Li, J. K.; Jia, Q. Y.; Stamatin, S.; Harrington, G. F.; Lyth, S. M.; Krtil, P.; Mukerjee, S. et al. Identification of catalytic sites in cobalt-nitrogen-carbon materials for the oxygen reduction reaction. *Nat. Commun.* **2017**, *8*, 957.

[10] Li, X. Y.; Rong, H. P.; Zhang, J. T.; Wang, D. S.; Li, Y. D. Modulating the local coordination environment of single-atom catalysts for enhanced catalytic performance. *Nano Res.* **2020**, *13*, 1842–1855.

[11] Sa, Y. J.; Seo, D. J.; Woo, J.; Lim, J. T.; Cheon, J. Y.; Yang, S. Y.; Lee, J. M.; Kang, D.; Shin, T. J.; Shin, H. S. et al. A general approach to preferential formation of active Fe-N_x sites in Fe–N/C

electrocatalysts for efficient oxygen reduction reaction. *J. Am. Chem. Soc.* **2016**, *138*, 15046–15056.
[12] Li, J.; Chen, S. G.; Yang, N.; Deng, M. M.; Ibraheem, S.; Deng, J. H.; Li, J.; Li, L.; Wei, Z. D. Ultrahigh-loading zinc single-atom catalyst for highly efficient oxygen reduction in both acidic and alkaline media. *Angew. Chem., Int. Ed.* **2019**, *58*, 7035–7039.
[13] Yan, X. X.; Liu, K. X.; Wang, T.; You, Y.; Liu, J. G.; Wang, P.; Pan, X. Q.; Wang, G. F.; Luo, J.; Zhu, J. Atomic interpretation of high activity on transition metal and nitrogen-doped carbon nanofibers for catalyzing oxygen reduction. *J. Mater. Chem. A.* **2017**, *5*, 3336–3345.
[14] Li, Y. J.; Ding, Y. J.; Zhang, B.; Huang, Y. C.; Qi, H. F.; Das, P.; Zhang, L. Z.; Wang, X.; Wu, Z. S.; Bao, X. H. N,O symmetric double coordination of an unsaturated Fe single-atom confined within a graphene framework for extraordinarily boosting oxygen reduction in Zn-air batteries. *Energy Environ. Sci.* **2023**, *16*, 2629–2636.
[15] Mehmood, A.; Gong, M. J.; Jaouen, F.; Roy, A.; Zitolo, A.; Khan, A.; Sougrati, M. T.; Primbs, M.; Bonastre, A. M.; Fongalland, D. et al. High loading of single atomic iron sites in Fe-NC oxygen reduction catalysts for proton exchange membrane fuel cells. *Nat. Catal.* **2022**, *5*, 311–323.
[16] Ren, X. Y.; Liu, H.; Wang, J. G.; Yu, J. Y. Electrospinning-derived functional carbon-based materials for energy conversion and storage. *Chin. Chem. Lett.* **2024**, *35*, 109282.
[17] Wang, X. X.; Cullen, D. A.; Pan, Y. T.; Hwang, S.; Wang, M. Y.; Feng, Z. X.; Wang, J. Y.; Engelhard, M. H.; Zhang, H. G.; He, Y. H. et al. Nitrogen-coordinated single cobalt atom catalysts for oxygen reduction in proton exchange membrane fuel cells. *Adv. Mater.* **2018**, *30*, 1706758.
[18] Ren, Y. J.; Tang, Y.; Zhang, L. L.; Liu, X. Y.; Li, L.; Miao, S.; Su, D. S.; Wang, A. Q.; Li, J.; Zhang, T. Unraveling the coordination structure-performance relationship in Pt_1/Fe_2O_3 single-atom catalyst. *Nat. Commun.* **2019**, *10*, 4500.
[19] Yuan, K.; Lützenkirchen-Hecht, D.; Li, L. B.; Shuai, L.; Li, Y. Z.; Cao, R.; Qiu, M.; Zhuang, X. D.; Leung, M. K. H.; Chen, Y. W. et al. Boosting oxygen reduction of single iron active sites via geometric and electronic engineering: Nitrogen and phosphorus dual coordination. *J. Am. Chem. Soc.* **2020**, *142*, 2404–2412.
[20] Zhang, J. Q.; Zhao, Y. F.; Chen, C.; Huang, Y. C.; Dong, C. L.; Chen, C. J.; Liu, R. S.; Wang, C. Y.; Yan, K.; Li, Y. D. et al. Tuning the coordination environment in single-atom catalysts to achieve highly efficient oxygen reduction reactions. *J. Am. Chem. Soc.* **2019**, *141*, 20118–20126.
[21] Chen, K. J.; Liu, K.; An, P. D.; Li, H. J. W.; Lin, Y. Y.; Hu, J. H.; Jia, C. K.; Fu, J. W.; Li, H. M.; Liu, H. et al. Iron phthalocyanine with coordination induced electronic localization to boost oxygen reduction reaction. *Nat. Commun.* **2020**, *11*, 4173.
[22] Shang, H. S.; Zhou, X. Y.; Dong, J. C.; Li, A.; Zhao, X.; Liu, Q. H.; Lin, Y.; Pei, J. J.; Li, Z.; Jiang, Z. L. et al. Engineering unsymmetrically coordinated $Cu\text{-}S_1N_3$ single atom sites with enhanced oxygen reduction activity. *Nat. Commun.* **2020**, *11*, 3049.
[23] Tang, C.; Jiao, Y.; Shi, B. Y.; Liu, J. N.; Xie, Z. H.; Chen, X.; Zhang, Q.; Qiao, S. Z. Coordination tunes selectivity: Two-electron oxygen reduction on high-loading molybdenum single-atom catalysts. *Angew. Chem., Int. Ed.* **2020**, *59*, 9171–9176.
[24] Zhang, H. B.; Liu, G. G.; Shi, L.; Ye, J. H. Single-atom catalysts: Emerging multifunctional materials in heterogeneous catalysis. *Adv. Energy Mater.* **2018**, *8*, 1701343.
[25] Seh, Z. W.; Kibsgaard, J.; Dickens, C. F.; Chorkendorff, I. B.; Nørskov, J. K.; Jaramillo, T. F. Combining theory and experiment in electrocatalysis: Insights into materials design. *Science.* **2017**, *355*, eaad4998.
[26] Liu, J. Y. Catalysis by supported single metal atoms. *ACS Catal.* **2017**, *7*, 34–59.
[27] Cao, J.; Zhang, D. Z.; Ren, B. Q.; Song, P.; Xu, W. L. Mn incorporated RuO_2 nanocrystals as an efficient and stable bifunctional electrocatalyst for oxygen evolution reaction and hydrogen evolution reaction in acid and alkaline. *Chin. Chem. Lett.* **2024**, *35*, 109863.
[28] Long, X. D.; Li, Z. L.; Gao, G.; Sun, P.; Wang, J.; Zhang, B. S.; Zhong, J.; Jiang, Z.; Li, F. W. Graphitic phosphorus coordinated single Fe atoms for hydrogenative transformations. *Nat. Commun.* **2020**, *11*, 4074.
[29] Haile, A. S.; Hansen, H. A.; Yohannes, W.; Mekonnen, Y. S. The role of nitrogen and sulfur dual coordination of cobalt in $Co\text{–}N_{4-x}S_x/C$ single atom catalysts in the oxygen reduction reaction. *Sustain. Energy Fuels.* **2022**, *6*, 179–187.
[30] Wang, X. Q.; Chen, Z.; Zhao, X. Y.; Yao, T.; Chen, W. X.; You, R.; Zhao, C. M.; Wu, G.; Wang, J.; Huang, W. et al. Regulation of coordination number over single Co sites: Triggering the efficient electroreduction of CO_2. *Angew. Chem., Int. Ed.* **2018**, *57*, 1944–1948.
[31] Wan, J. W.; Zhao, Z. H.; Shang, H. S.; Peng, B.; Chen, W. X.; Pei, J. J.; Zheng, L. R.; Dong, J. C.; Cao, R.; Sarangi, R. et al. *In situ* phosphatizing of triphenylphosphine encapsulated within metal-organic frameworks to design atomic $Co_1\text{-}P_1N_3$ interfacial structure for promoting catalytic performance. *J. Am. Chem. Soc.* **2020**, *142*, 8431–8439.
[32] Yan, C. C.; Li, H. B.; Ye, Y. F.; Wu, H. H.; Cai, F.; Si, R.; Xiao, J. P.; Miao, S.; Xie, S. H.; Yang, F. et al. Coordinatively unsaturated nickel–nitrogen sites towards selective and high-rate CO_2 electroreduction. *Energy Environ. Sci.* **2018**, *11*, 1204–1210.
[33] Hu, K. S.; Zhang, Y. L.; Zhu, J. Y.; Mai, J.; Liu, G.; Sugumar, M. K.; Liu, X. H.; Zhan, F.; Tan, R. Nano-engineered catalysts for high-performance oxygen reduction reaction. *Chin. Chem. Lett.* **2024**, *35*, 109423.
[34] Osmieri, L.; Monteverde Videla, A. H. A.; Ocón, P.; Specchia, S. Kinetics of oxygen electroreduction on Me-N-C (Me = Fe, Co, Cu) catalysts in acidic medium: Insights on the effect of the transition metal. *J. Phys. Chem. C* **2017**, *121*, 17796–17817.
[35] Zitolo, A.; Goellner, V.; Armel, V.; Sougrati, M. T.; Mineva, T.; Stievano, L.; Fonda, E.; Jaouen, F. Identification of catalytic sites for oxygen reduction in iron- and nitrogen-doped graphene materials. *Nat. Mater.* **2015**, *14*, 937–942.
[36] Ramaswamy, N.; Tylus, U.; Jia, Q. Y.; Mukerjee, S. Activity descriptor identification for oxygen reduction on nonprecious electrocatalysts: Linking surface science to coordination chemistry. *J. Am. Chem. Soc.* **2013**, *135*, 15443–15449.
[37] Lu, Z. Y.; Wang, J.; Huang, S. F.; Hou, Y. L.; Li, Y. G.; Zhao, Y. P.; Mu, S. C.; Zhang, J. J.; Zhao, Y. F. N,B-codoped defect-rich graphitic carbon nanocages as high performance multifunctional electrocatalysts. *Nano Energy* **2017**, *42*, 334–340.
[38] Chi, K.; Wang, Z. P.; Sun, T.; He, P.; Xiao, F.; Lu, J.; Wang, S. Simultaneously engineering the first and second coordination shells of single iron catalysts for enhanced oxygen reduction. *Small* **2024**, *20*, 2311817.
[39] Xu, Q.; Guo, C. X.; Tian, S. B.; Zhang, J.; Chen, W. X.; Cheong, W. C.; Gu, L.; Zheng, L. R.; Xiao, J. P.; Liu, Q. et al. Coordination structure dominated performance of single-atomic Pt catalyst for anti-Markovnikov hydroboration of alkenes. *Sci. China Mater.* **2020**, *63*, 972–981.
[40] Jiang, H. L.; Liu, B.; Lan, Y. Q.; Kuratani, K.; Akita, T.; Shioyama, H.; Zong, F. Q.; Xu, Q. From metal-organic framework to nanoporous carbon: Toward a very high surface area and hydrogen uptake. *J. Am. Chem. Soc.* **2011**, *133*, 11854–11857.
[41] Zhang, H. G.; Hwang, S.; Wang, M. Y.; Feng, Z. X.; Karakalos, S.; Luo, L. L.; Qiao, Z.; Xie, X. H.; Wang, C. M.; Su, D. et al. Single atomic iron catalysts for oxygen reduction in acidic media: Particle size control and thermal activation. *J. Am. Chem. Soc.* **2017**, *139*, 14143–14149.
[42] Xiao, M. L.; Chen, Y. T.; Zhu, J. B.; Zhang, H.; Zhao, X.; Gao, L. Q.; Wang, X.; Zhao, J.; Ge, J. J.; Jiang, Z. et al. Climbing the apex of the ORR volcano plot via binuclear site construction: Electronic and geometric engineering. *J. Am. Chem. Soc.* **2019**, *141*, 17763–17770.

[43] Chen, W. X.; Pei, J. J.; He, C. T.; Wan, J. W.; Ren, H. L.; Zhu, Y. Q.; Wang, Y.; Dong, J. C.; Tian, S. B.; Cheong, W. C. et al. Rational design of single molybdenum atoms anchored on N-doped carbon for effective hydrogen evolution reaction. *Angew. Chem., Int. Ed.* **2017**, *56*, 16086–16090.

[44] Chen, G. B.; Lu, R. H.; Li, C. Z.; Yu, J. M.; Li, X. D.; Ni, L. M.; Zhang, Q.; Zhu, G. Q.; Liu, S. W.; Zhang, J. X. et al. Hierarchically porous carbons with highly curved surfaces for hosting single metal FeN_4 sites as outstanding oxygen reduction catalysts. *Adv. Mater.* **2023**, *35*, 2300907.

[45] Liu, F. X.; Zou, X.; Yue, N. L.; Zhang, W.; Zheng, W. T. Correlative Raman imaging and scanning electron microscopy for advanced functional materials characterization. *Cell Rep. Phys. Sci.* **2023**, *4*, 101607.

[46] Jiang, Z. L.; Sun, W. M.; Shang, H. S.; Chen, W. X.; Sun, T. T.; Li, H. J.; Dong, J. C.; Zhou, J.; Li, Z.; Wang, Y. et al. Atomic interface effect of a single atom copper catalyst for enhanced oxygen reduction reactions. *Energy Environ. Sci.* **2019**, *12*, 3508–3514.

[47] Pei, J. J.; Shang, H. S.; Mao, J. J.; Chen, Z.; Sui, R.; Zhang, X. J.; Zhou, D. N.; Wang, Y.; Zhang, F.; Zhu, W. et al. A replacement strategy for regulating local environment of single-atom Co-S_xN_{4-x} catalysts to facilitate CO_2 electroreduction. *Nat. Commun.* **2024**, *15*, 416.

[48] Luo, X.; Wei, X. Q.; Wang, H. J.; Gu, W. L.; Kaneko, T.; Yoshida, Y.; Zhao, X.; Zhu, C. Z. Secondary-atom-doping enables robust Fe–N–C single-atom catalysts with enhanced oxygen reduction reaction. *Nano-Micro Lett.* **2020**, *12*, 163.

[49] Kone, I.; Xie, A.; Tang, Y.; Chen, Y.; Liu, J.; Chen, Y. M.; Sun, Y. Z.; Yang, X. J.; Wan, P. Y. Hierarchical porous carbon doped with iron/nitrogen/sulfur for efficient oxygen reduction reaction. *ACS Appl. Mater. Interfaces* **2017**, *9*, 20963–20973.

[50] Vilé, G.; Sharma, P.; Nachtegaal, M.; Tollini, F.; Moscatelli, D.; Sroka-Bartnicka, A.; Tomanec, O.; Petr, M.; Filip, J.; Pieta, I. S. et al. An earth-abundant Ni-based single-atom catalyst for selective photodegradation of pollutants. *Solar RRL* **2021**, *5*, 2100176.

[51] Qiu, P. X.; Chen, H.; Xu, C. M.; Zhou, N.; Jiang, F.; Wang, X.; Fu, Y. S. Fabrication of an exfoliated graphitic carbon nitride as a highly active visible light photocatalyst. *J. Mater. Chem. A* **2015**, *3*, 24237–24244.

[52] Safaei, J.; Mohamed, N. A.; Noh, M. F. M.; Soh, M. F.; Riza, M. A.; Mustakim, N. S. M.; Ludin, N. A.; Ibrahim, M. A.; Isahak, W. N. R. W.; Teridi, M. A. M. Facile fabrication of graphitic carbon nitride, (g-C_3N_4) thin film. *J. Alloy. Compd.* **2018**, *769*, 130–135.

[53] Qin, T. T.; Zhang, W. L.; Ma, Y.; Zhang, W.; Dong, T. W.; Chu, X. Y.; Li, T.; Wang, Z. Z.; Yue, N. L.; Liu, H. Y. et al. Mechanistic insights into the electrochemical Li/Na/K-ion storage for aqueous bismuth anode. *Energy Storage Mater.* **2022**, *45*, 33–39.

[54] Zhou, X. Y.; Qiao, S. F.; Yue, N. L.; Zhang, W.; Zheng, W. T. Soft X-ray emission spectroscopy finds plenty of room in exploring lithium-ion batteries. *Mater. Res. Lett.* **2023**, *11*, 239–249.

[55] Yang, Y.; Li, B.; Liang, Y. N.; Ni, W. P.; Li, X.; Shen, G. Z.; Xu, L.; Chen, Z. J.; Zhu, C.; Liang, J. X. et al. Hetero-diatomic CoN_4–NiN_4 site pairs with long-range coupling as efficient bifunctional catalyst for rechargeable Zn-air batteries. *Adv. Sci.* **2024**, *11*, 2310231.

[56] Chen, C. L.; Chai, J.; Sun, M. R.; Guo, T. Q.; Lin, J.; Zhou, Y. R.; Sun, Z. Y.; Zhang, F.; Zhang, L.; Chen, W. X. et al. An asymmetrically coordinated ZnCoFe hetero-trimetallic atom catalyst enhances the electrocatalytic oxygen reaction. *Energy Environ. Sci.* **2024**, *17*, 2298–2308.

[57] Xu, Y. H.; Yao, Z. Q.; Mao, Z. C.; Shi, M. Q.; Zhang, X. Y.; Cheng, F.; Yang, H. B.; Tao, H. B.; Liu, B. Single-Ni-atom catalyzes aqueous phase electrochemical reductive dechlorination reaction. *Appl. Catal. B: Environ.* **2020**, *277*, 119057.

[58] Hu, X.; Chen, S. Y.; Chen, L. T.; Tian, Y.; Yao, S.; Lu, Z. Y.; Zhang, X.; Zhou, Z. What is the real origin of the activity of Fe-N-C electrocatalysts in the O_2 reduction reaction. Critical roles of coordinating pyrrolic n and axially adsorbing species. *J. Am. Chem. Soc.* **2022**, *144*, 18144–18152.

[59] Zhang, N.; Zhou, T. P.; Chen, M. L.; Feng, H.; Yuan, R. L.; Zhong, C. A.; Yan, W. S.; Tian, Y. C.; Wu, X. J.; Chu, W. S. et al. High-purity pyrrole-type FeN_4 sites as a superior oxygen reduction electrocatalyst. *Energy Environ. Sci.* **2020**, *13*, 111–118.

[60] Yang, L.; Cheng, D. J.; Xu, H. X.; Zeng, X. F.; Wan, X.; Shui, J. L.; Xiang, Z. H.; Cao, D. P. Unveiling the high-activity origin of single-atom iron catalysts for oxygen reduction reaction. *Proc. Natl. Acad. Sci. USA* **2018**, *115*, 6626–6631.

[61] Guo, S. T.; Li, R.; Tian, F. Z.; Yang, X. T.; Wang, L.; Guan, S. Y.; Zhou, S. Y.; Lu, J. Carbon-defect-driven boron carbide for dual-modal NIR-II/photoacoustic imaging and photothermal therapy. *ACS Biomater. Sci. Eng.* **2021**, *7*, 3370–3378.

[62] Nsanzimana, J. M. V.; Gong, L. Q.; Dangol, R.; Reddu, V.; Jose, V.; Xia, B. Y.; Yan, Q. Y.; Lee, J. M.; Wang, X. Tailoring of metal boride morphology via anion for efficient water oxidation. *Adv. Energy Mater.* **2019**, *9*, 1901503.

[63] Xie, F.; Sun, L.; Qian, J. L.; Shi, X. C.; Hu, J. J.; Qu, Y. R.; Tan, H. K.; Wang, K.; Zhang, Y. H. Polypyrrole-coated Boron-doped Nickel–Cobalt sulfide on electrospinning carbon nanofibers for high performance asymmetric supercapacitors. *J. Colloid. Interface Sci.* **2022**, *628*, 371–383.

[64] Li, J. C.; Meng, Y.; Zhang, L. L.; Li, G. Z.; Shi, Z. C.; Hou, P. X.; Liu, C.; Cheng, H. M.; Shao, M. H. Dual-phasic carbon with Co single atoms and nanoparticles as a bifunctional oxygen electrocatalyst for rechargeable Zn-air batteries. *Adv. Funct. Mater.* **2021**, *31*, 2103360.

[65] Wang, X. K.; Zhou, X. K.; Li, C.; Yao, H. X.; Zhang, C.; Zhou, J.; Xu, R.; Chu, L.; Wang, H. L.; Gu, M. et al. Asymmetric Co-N_3P_1 trifunctional catalyst with tailored electronic structures enabling boosted activities and corrosion resistance in an uninterrupted seawater splitting system. *Adv. Mater.* **2022**, *34*, 2204021.

[66] Sun, K.; Huang, Y.; Wang, Q. Y.; Zhao, W. D.; Zheng, X. S.; Jiang, J.; Jiang, H. L. Manipulating the spin state of Co sites in metal-organic frameworks for boosting CO_2 photoreduction. *J. Am. Chem. Soc.* **2024**, *146*, 3241–3249.

[67] Song, K. X.; Yang, B. B.; Zou, X.; Zhang, W.; Zheng, W. T. Unified ORR mechanism criteria via charge-spin-coordination of Fe functional units. *Energy Environ. Sci.* **2024**, *17*, 27–48.

[68] Chen, Q. Y.; Chen, Z. Y.; Ali, A.; Luo, Y. Q.; Feng, H. Y.; Luo, Y. Y.; Tsiakaras, P.; Kang Shen, P. Shell-thickness-dependent Pd@PtNi core-shell nanosheets for efficient oxygen reduction reaction. *Chem. Eng. J.* **2022**, *427*, 131565.